Space Weather

RESEARCH ARTICLE
10.1029/2020SW002645

Special Section:
Small Satellites for Space Weather Research and Forecasting Workshops

Upper-Atmosphere Mass Density Variations From CASSIOPE Precise Orbits

Andrés Calabia[1,2] and **Shuanggen Jin**[1,3]

[1]School of Remote Sensing and Geomatics Engineering, Nanjing University of Information Science and Technology, Nanjing, China, [2]School of Land Surveying, Geodesy and Mapping Engineering, Universidad Politécnica de Madrid, Madrid, Spain, [3]Shanghai Astronomical Observatory, Chinese Academy of Sciences, Shanghai, China

Abstract Thermospheric mass density (TMD) measurements are invaluable to accurately estimate and predict the position and velocity of orbiting objects in Low Earth Orbit (LEO). Existing observational methods and predictive models have some problems (e.g., accuracy, resolution, coverage, cost, etc.) to describe and forecast the actual air drag variations as required for practical applications. With the increasing number of LEO satellites equipped with high-precision Global Navigation Satellite System (GNSS) receivers, the precise orbits can be used to obtain non-gravitational accelerations, and therefore estimate TMD variations. In this study, TMD is estimated from the precise orbits of CAScade SmallSat and IOnospheric Polar Explorer (CASSIOPE) at one-second time step, and the TMD variations following the February 2014 geomagnetic storm are investigated. Using this method, a more detailed description than previous methods and empirical models is given with short-term TMD variations during geomagnetic storm conditions. The empirical model NRLMSISE-00 shows less pronounced and more averaged variations, while CASSIOPE-derived TMD can reflect the abrupt disturbances triggered by the geomagnetic storm. CASSIOPE TMD shows a correlation of 72.4% to the merging electric field E_m index, while the NRLMSISE-00 model shows a correlation of 42.1%.

Key Points:

- Thermospheric mass densities are estimated from CAScade SmallSat and IOnospheric Polar Explorer precise orbits
- The detailed thermospheric mass density responses are obtained during the February 2014 geomagnetic storm
- CASSIOPE-derived thermospheric mass density is better than the NRLMSIS-00 model to reflect responses to the storm

Correspondence to:
S. Jin,
sgjin@nuist.edu.cn;
sg.jin@yahoo.com

Citation:
Calabia, A., & Jin, S. (2021). Upper-atmosphere mass density variations from CASSIOPE precise orbits. *Space Weather*, *19*, e2020SW002645. https://doi.org/10.1029/2020SW002645

Received 6 OCT 2020
Accepted 29 MAR 2021

Author Contributions:
Conceptualization: Andrés Calabia
Data curation: Andrés Calabia
Formal analysis: Andrés Calabia
Funding acquisition: Shuanggen Jin
Investigation: Andrés Calabia
Methodology: Andrés Calabia
Project Administration: Shuanggen Jin
Software: Andrés Calabia
Supervision: Shuanggen Jin
Validation: Andrés Calabia
Visualization: Andrés Calabia

1. Introduction

Low Earth Orbit (LEO) satellites are significantly affected by variable air drag forces, which are mainly altered by atmospheric expansion/contraction driven by solar and geomagnetic activity. Air drag reduces the orbital velocity of a satellite, its nominal altitude, and shortens its lifespan. The effect of air drag pressure on the position of a satellite orbiting at an altitude of around 450 km may drag around 3 m per revolution in the along-track axis, limiting the satellite's lifespan to approximately 5–10 years. In applications, such as remote sensing or satellite altimetry and gravity, the orbital trajectory and velocity (ephemeris) of satellites must be known to an accuracy of a few millimeters. Moreover, the exponential increase in presence of space debris (consider the recent destructive events of Fengyun-1C, Iridium, and Mission Shakti) has highlighted the importance of orbital tracking and prediction of potential collisions. The dynamic Precise Orbit Determination (POD) method tracks and predicts the orbital ephemeris by calculating an orbital trajectory through a double integration and linearization of Newton-Euler's equation of motion (Montenbruck & Gill, 2013). In the POD method, by combining force models with empirical observations, used for example in laser-ranging, Doppler, accelerometer, or Global Navigation Satellite System (GNSS) measurements, the position, and velocity of a satellite can be stochastically estimated with significant accuracy (Jin & Su, 2020; Tapley et al., 2004).

Due to variable air drag force being so important, in the last decade, thermospheric mass density (TMD) variations driven by solar and geomagnetic activity have been investigated using satellite technology to a great extent (e.g., Calabia & Jin, 2016, 2019; Chen et al., 2014; Cnossen & Förster, 2016; Doornbos et al., 2010; Emmert & Picone, 2010; Ercha et al., 2012; Guo et al., 2016; Lei et al., 2010, 2012; H. Liu et al., 2009; R. Liu et al., 2010, 2011; Müller et al., 2009; Panzetta et al., 2018; Sutton et al., 2009). But these studies have in turn exposed the limitations of the existing empirical models (e.g., JB2008 [Bowman et al., 2008], DTM [Bruinsma, 2015], NRLMSISE-00 [Picone et al., 2002]) in accurately predicting TMD variations, especially during geomagnetic storm conditions. The resulting positioning errors, from these limitations, affect the POD accuracy so significantly, they fail to meet the operational requirements for precise orbital tracking (Anderson et al., 2009; Calabia et al., 2020). This is largely due to the limited quality and quantity of observations used

Writing – original draft: Andrés Calabia
Writing – review & editing: Andrés Calabia, Shuanggen Jin

to better measure the TMD variability, and the lack of comprehensive approaches to calibrate the models (Emmert, 2015; Jin et al., 2018).

For example, accelerometer-based TMD estimates are very sensitive and globally distributed (usually at a second interval along orbits), but the measurement method is very expensive, has a low revisiting-time, calibration difficulties to estimate the actual TMD, and only a few missions have provided good data, viz. Challenging Minisatellite Payload (CHAMP) (Bruinsma et al., 2004; Sutton et al., 2007), Gravity Recovery and Climate Experiment (GRACE) (Calabia, 2016; Doornbos, 2012; Sutton, 2008), Gravity field and steady-state ocean circulation explorer (GOCE) (Bruinsma et al., 2014), and Swarm (Siemes et al., 2016). Note that the original purpose of these missions was not the estimation of in situ TMD. Other methods also have their drawbacks varying in problems with accuracy, resolution, coverage, revisiting-time, calibration, complexity, and so on. A list of the existing measurement methods includes the semi-major axis variation method (Picone et al., 2005), the stochastic TMD estimation within the POD approaches (IJssel & Visser, 2007; Kuang et al., 2014; McLaughlin et al., 2013; Visser et al., 2013), mass spectrometers (Tang et al., 2020), incoherent scatter radars (Nicolls et al., 2014), Broglio drag balance instruments (Santoni et al., 2010), miniaturized pressure gauge instruments (Clemmons et al., 2008), ultraviolet remote sensing (Meier & Picone, 1994; Meier et al., 2015), and the techniques of atmospheric occultation (Aikin et al., 1993; Determan et al., 2007). Nowadays, with the increasing number of LEO satellites equipped with high-precision GNSS receivers, the precise orbits can be used to obtain non-gravitational accelerations at a high resolution, and therefore estimate TMD variations (Calabia & Jin, 2017).

Geomagnetic storms cause large and abrupt TMD increases lasting from several hours to several days (Calabia & Jin, 2019), while the existing observational methods and empirical models fail to describe and predict these TMD variations with enough resolution and accuracy. Previous studies using the acceleration approach have attempted to stochastically estimate high-frequency TMD variations within the POD method (e.g., IJssel, 2014; IJssel & Visser, 2007; Kuang et al., 2014), but their results showed too low resolution with a unique solution in each estimation interval (~20 min) to study high-frequency disturbances caused by, for example, geomagnetic storms (Liangliang et al., 2019). For this work, TMD is calculated along CASCade SmallSat and IOnospheric Polar Explorer (CASSIOPE) precise orbits at one-second time step, and the density responses to the February 2014 geomagnetic storm are investigated and evaluated. A more detailed discussion in view of the achieved accuracy along the elliptic orbit is given in the following sections.

2. Data and Methods

2.1. CASSIOPE Precise Orbit Data

The CASSIOPE spacecraft was launched on September 29, 2013, into a slightly eccentric polar orbit of 81° inclination with a perigee of approximately 325 km altitude and an apogee near 1,500 km altitude. While previous commercial-off-the-shelf GNSS receivers have provided limited accuracy, the CASSIOPE satellite has demonstrated its full capability for geodetic observations at an affordable cost in low-budget space missions (Kim & Langley, 2019). The CASSIOPE satellite uses five commercial-off-the-shelf, geodetic grade, dual-frequency GPS receivers L1 C/A and L2 P(Y) tracking up to 12 satellites, to be used for high precision navigation, attitude determination, time synchronization, and radio occultation measurements. The precise orbit solutions at a second interval were computed by Montenbruck et al. (2019) in a reduced-dynamic approach with float-ambiguity estimation using the ionosphere-free linear combination of dual-frequency code and carrier phase observations. Associated imperfections in the density and drag model were compensated through piecewise constant empirical accelerations with zero a priori values. This strategy allows counterbalancing both the disadvantages of the GNSS measurement noises and the uncertainties in the models.

2.2. Calculation of Air Drag Acceleration

Non-gravitational accelerations acting on LEO satellites mainly include air drag and irradiative accelerations. The method proposed in (Calabia et al., 2015) computes instantaneous total accelerations through numerical differentiation of the precise velocities so that the "observed" air drag accelerations acting on the satellite are obtained by removing the gravitational and radiation pressure accelerations at each satellite's

Table 1
Gravitational Force Models Used in This Study

Models	Details
Earth gravity	EGM2008 with low degree rates. Degree 120. Petit and Luzum (2010).
Third bodies	Moon and Sun from JPL DE421. Montenbruck and Gill (2013).
Earth tides	Due to Moon and Sun, Wahr terms. Petit and Luzum (2010).
Ocean tides	EOT11a (256 tides). Degree 120. Mayer-Gürr et al. (2012).
Solid Earth pole tide	IERS 2010 using sub-daily wobble variables. Petit and Luzum (2010).
Ocean pole tide	From Desai (2002) using sub-daily wobble variables. Degree 120.
Relativity	Schwarzschild correction. Petit and Luzum (2010).

position. As recommended by the authors, the 8-data point piece-wise Lagrange interpolation and a time-interval of 0.05 s are suggested for the numerical differentiation. These settings limit the bias error in the numerical differentiation (arc-to-chord threshold approach) to approximately 10^{-9} m/s^2.

Table 1 summarizes the gravitational force models used in this study. The conventional gravity model is based on the EGM2008 with the underlying background for the secular variations (Petit & Luzum, 2010). We employ the EOT11a ocean tides of Mayer-Gürr et al. (2012), the ocean pole tide of Desai (2002), and the third body tide caused by the Moon and Sun are calculated with the Jet Propulsion Laboratory (JPL) DE421 ephemeris following the indications of Montenbruck and Gill (2013). Time-varying Stokes' coefficients up to a degree and order of 120 are computed (including sub-daily variations) with an increment of time small enough (~3,600 s) to desensitize from discontinuities in the resulting non-gravitational accelerations. We employ the first derivative of the gravitational potential in Cartesian coordinates (Frommknecht, 2008) to compute the gravity at each epoch along the CASSIOPE orbits. The transformations between reference-systems follow the conventions of Petit and Luzum (2010).

Irradiative accelerations mainly include the direct solar radiation, the radiation reflected at the Earth's surface, and the Earth's infrared radiation. While the Earth's infrared radiation (long-wave radiation) is almost independent of illumination conditions, the other two solar radiations (short-wave radiation) must account for the planetary eclipse ratio (Montenbruck & Gill, 2013). On the plates of the user's satellite, one part of the incoming radiation is absorbed and the other is reflected diffusely and specularly. Luthcke et al. (1997) formulated the entire resultant force on the satellite due to the solar radiation, which accounts for each satellite's plate areas and their orientation, its coefficients of diffusive (c_{rd}) and specular (c_{rs}) reflectivity, and the mass of the satellite (the CASSIOPE satellite has a mass of approximately 500 kg). The Earth's infrared radiation is computed following the indications of Knocke and Ries (1987), and the reflected radiant flux is calculated with the monthly averages of NASA's Total Ozone Mapping Spectrometer (TOMS) reflectivity index following the indications of Bhanderi (2005). For these calculations, the geometry model of the CASSIOPE spacecraft is given in Figure 1, and its surface properties are given in Table 2. Additional details can be found in Montenbruck et al. (2019). Detailed algorithms and accurate schemes to estimate irradiative accelerations can be found in numerous works, for example, Vielberg and Kusche (2020), Wöske et al. (2019), Jin et al. (2018), Calabia and Jin (2017), Doornbos (2012), Sutton et al. (2007).

2.3. Estimation of TMD

TMD estimates are computed using the drag-force (F_D) formula (Newton, 1726):

$$F_D = a_D m = \frac{1}{2} C_D A \rho v_r^2. \quad (1)$$

In this equation, a_D is the acceleration due to air drag, m is the mass of the satellite, C_D is the drag coefficient, ρ is the TMD, and A is the cross-sectional area perpendicular to the relative velocity of the atmosphere with respect to the spacecraft v_r, which includes the co-rotating atmosphere and the horizontal winds. Horizontal wind velocities are calculated from the horizontal wind model HWM14 (Drob et al., 2015), and

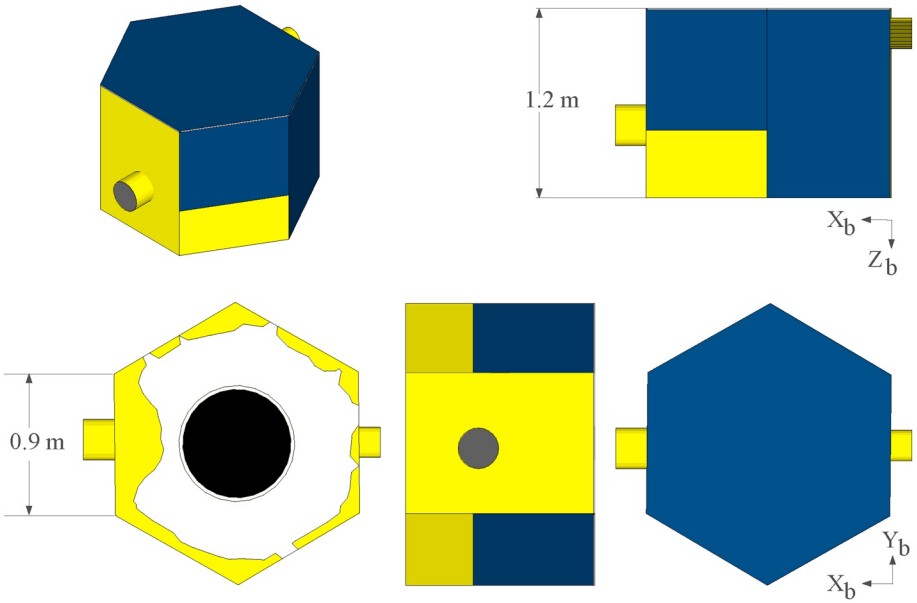

Figure 1. Geometry model of the CASSIOPE spacecraft in the satellite's body reference system (X_b, Y_b, Z_b). CASSIOPE, CAScade SmallSat and IOnospheric Polar Explorer.

the velocity of the co-rotating atmosphere is computed as the vector product between the Earth's angular rotation and the satellite's position vector.

Unfortunately, Equation 1 is incomplete, since both ρ and C_D are usually unknown parameters. The accurate estimation of C_D for LEO satellites is still a challenge (e.g., March et al., 2019; Mehta et al., 2014), and the lack of direct measurements complicates the estimation of the actual TMD. Estimating C_D of LEO satellites depends on many factors, including energy accommodation, gas-surface interaction, molecular reflections distribution, atmospheric compositions and temperature, and satellite geometry, speed, attitude, temperature, composition, and so on. However, by using an approximation of the actual C_D value, the results from Equation 1 can provide estimates of the relative variations of TMD, which are very valuable to describe and localize in detail short-term disturbances caused by, for example, geomagnetic storms. Then,

Table 2
Surface Properties for the CASSIOPE Spacecraft

Panel	Area(m^2)	X_b	Y_b	Z_b	Material	c_{rs} VIS	c_{rd} VIS	c_{rs} IR	c_{rd} IR
Zenit	2.1	0	0	−1	Si glass-solar array	0.05	0.30	0.03	0.16
Nadir 1	1.2	0	0	+1	Teflon	0.68	0.20	0.19	0.06
Nadir 2	0.6	0	0	+1	SiOx/Kapton	0.40	0.26	0.23	0.15
Nadir 3	0.4	0	0	+1	Glass	0.05	0.30	0.03	0.16
Front	1.1	1	0	0	SiOx/Kapton	0.40	0.26	0.23	0.15
Rear	1.1	−1	0	0	SiOx/Kapton	0.40	0.26	0.23	0.15
Right/front 1	0.7	+0.86	+0.86	0	Si glass-solar array	0.05	0.30	0.03	0.16
Right/front 2	0.4	+0.86	+0.86	0	SiOx/Kapton	0.40	0.26	0.23	0.15
Right/rear	1.1	−0.86	0.86	0	Si glass-solar array	0.05	0.30	0.03	0.16
Left/front 1	0.7	−0.86	0.86	0	Si glass-solar array	0.05	0.30	0.03	0.16
Left/front 2	0.4	−0.86	0.86	0	SiOx/Kapton	0.40	0.26	0.23	0.15
Left/rear	1.1	−0.86	−0.86	0	Si glass-solar array	0.05	0.30	0.03	0.16

Note. For each surface, an estimate of the area, the components of its unit normal in the satellite reference system, the material, as well as its diffusive (c_{rd}) and specular (c_{rs}) reflectivity coefficients for the visible (VIS) and the infrared (IR) are provided.

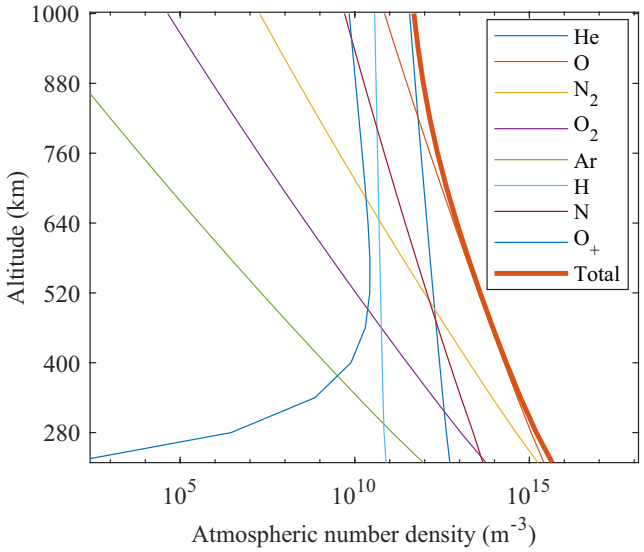

Figure 2. Principal constituents of the upper atmosphere at a random location ($\varphi = 45°S$, $\lambda = 180°E$) estimated by NRLMSISE-00 on February 15, 2014 at 0 h UT.

the NRLMSISE-00 semi-empirical model (Picone et al., 2002) can be used to assess for accuracy of the resulting estimates. Note that NRLMSISE-00 is based on averaged values from several measurement techniques, including mass spectrometers, incoherent scatter radars, satellite drag data, and solar ultraviolet occultation.

In this study, we approximate a variable C_D for CASSIOPE in terms of solar flux and altitude. The following assumptions are adopted. We first employ the C_D values provided by Pardini et al. (2006) for a spherical satellite, which are dependent on altitude and solar activity. Then, we adjust these values to the hexagonal-prism shape of CASSIOPE (Figure 1) with a scaling factor based on the work done by Walker et al. (2014), who estimated C_D values for different satellite shapes as a function of atmospheric number density. Since the orbit of CASSIOPE ranges altitudes from approximately 300 to 1,400 km, it is estimated that the maximum value of atmospheric number density for altitudes above 300 km is approximately 10^{15}.

3. Results and Analysis

3.1. Drag Coefficient for the CASSIOPE Spacecraft

Figure 2 shows NRLMSISE-00 estimates as a function of altitude for an arbitrary location. Walker et al. (2014) showed that for number density values below 10^{16} the drag coefficient for a spherical satellite is 2.2. Similarly, following the results of Walker et al. (2014), a value of approximately 2.3 is estimated for a satellite with a hexagonal-prism shape, analogous to that of CASSIOPE (slightly between a cube and a cylinder perpendicular to the flow). This corresponds to a drag coefficient ratio between a spherical satellite and a hexagonal-prism satellite of approximately 1.05. Following these hypotheses, all possible values of C_D are calculated, and TMD can be estimated using Equation 1. Figure 3 shows the resulting drag coefficient C_D for CASSIOPE as a function of altitude and solar activity, and the TMD results are shown in the next section.

3.2. TMD Estimation and Responses to the February 2014 Geomagnetic Storm

In February 2014, four powerful Earth-directed coronal mass ejections (CMEs) triggered a highly complex, multiphase geomagnetic storm. The first two CMEs arrived on 19 and 20 February, the other two arrived on 23 and 27 February. The corresponding TMD responses as seen by CASSIOPE and NRLMSISE-00 are analyzed in Figures 4 and 5, focusing first on the storm of 20 February and then a complete 15-day period, respectively. In these figures, the merging electric field E_m and the disturbance storm time Dst index are included to identify the progress of the events. It is well known that these two indices can represent with high resolution the TMD variations triggered by magnetospheric forcing (Calabia & Jin, 2019). Note that a minor storm ranges -30 nT > Dst > -50 nT, a moderate storm -50 nT > Dst > -100 nT, an intense storm -100 nT > Dst > -250 nT, and a great storm Dst < -250 nT (Gonzalez et al., 1999).

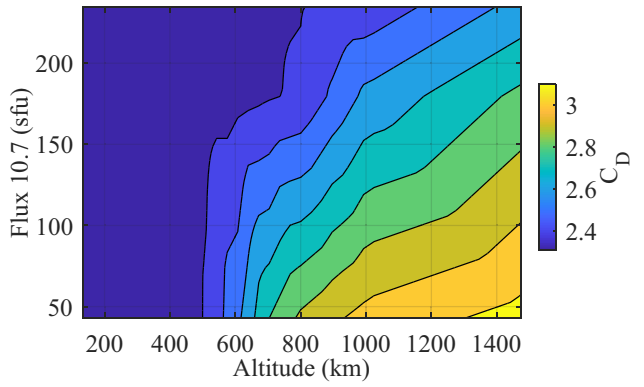

Figure 3. Drag coefficient for the CASSIOPE spacecraft as a function of altitude and solar activity. CASSIOPE, CAScade SmallSat and IOnospheric Polar Explorer.

The first storm started at 14:00 UT (universal time) on 18 February, showing a Dst drop down to -112 nT at 09:00 UT on 19 February. The second storm began around 04:00 UT on 20 February (blue circles in Figure 4c), showing a Dst drop from -40 nT down to -86 nT at 12:00 UT. The Dst index recovered rapidly up to -40 nT at 19:00 UT, and then gradually increased to 4 nT until the onset of the third storm at 08:00 UT on 23 February, followed to a minimum of -56 nT at 00:00 UT on 24 February. The last storm began at 16:00 UT on 27 February, showing a minimum Dst of -99 nT at 00:00 UT on 28 February.

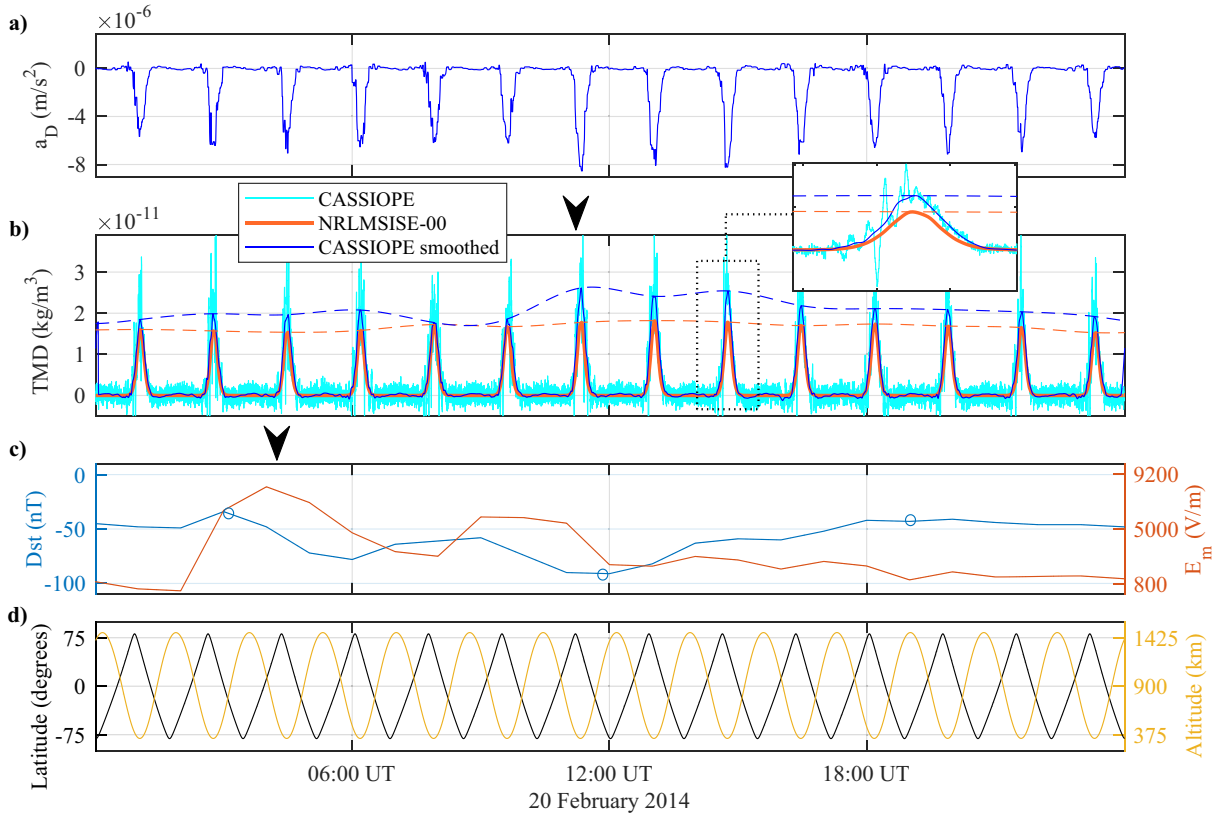

Figure 4. In (a), we show the drag acceleration (a_D) from CASSIOPE's precise orbits on February 20, 2014 (ϑ ≈ 13:00 LST). The corresponding TMD estimates (original and smoothed at 6 min mean-average running filter) along with the NRLMSISE-00 estimates are shown in (b). The upper bounds of TMD are plotted in dashed lines, the circles indicate the relative minimum and maximum values, and the arrowheads show the delay-time of approximately 6 h with respect to the maximum of the merging electric field E_m. In (c), we show the merging electric field E_m and the disturbance storm time Dst index. In (d), we include the orbit latitude and altitude of CASSIOPE. CASSIOPE, CAScade SmallSat and IOnospheric Polar Explorer; TMD, thermospheric mass density.

During this period, CASSIOPE's orbital descending node (ϑ) was approximately located at 13:00 Local Solar Time (LST), reaching its lowest altitude at approximately 62°N latitude (location of the orbital perigee). Figure 4d displays the latitude and altitude of the CASSIOPE's orbital trajectory, and Figure 4a shows the drag acceleration (a_D) calculated from CASSIOPE precise orbits on February 20, 2014 (see the Methods section, *Calculation of air drag acceleration* a_D). In this figure, enhanced air drag accelerations can be clearly seen a few hours after the storm, at 12:00 UT. The corresponding TMD estimates along with the estimates of the NRLMSISE-00 model are shown in Figure 4b. In this study, the CASSIOPE TMD estimates have been smoothed with a 6 min mean-average running filter to exclude signal-noises and outliers. Noises and outliers may be originated from errors induced in the stochastic POD solution, or even actual accelerations along the orbits (further study is required). Assuming that the TMD estimates above ~800 km altitude should be zero, that is, TMD estimate reflects only noise there, the standard deviation of the CASSIOPE estimates during this period, and for altitudes above 800 km, has shown to be 1.3×10^{-12} Kg/m^3. However, the actual error at lower altitudes would likely be larger due to the existence of other error sources, which are proportional to the TMD signal, for example, the drag coefficient. Future investigations will address the accuracy of a larger TMD data set, and the possible dependence of the errors to other factors, including altitude, latitude, LST, and annual and solar cycles.

The upper bounds of TMD (lowest altitude) are plotted in dashed lines for clarity (Figure 4), showing obvious differences between CASSIOPE and NRLMSISE-00 TMD estimates. NRLMSISE-00 shows less pronounced and more averaged variations, while CASSIOPE TMD can reflect the abrupt disturbances triggered by the geomagnetic storm, following the variations of the merging electric field E_m. The corresponding delay-time of approximately 7 h with the maximum of the merging electric field E_m (arrowheads) agrees well with the reported values in Calabia and Jin (2019). Figures 5a and 5b show the CASSIOPE and NRLMSISE-00 TMD

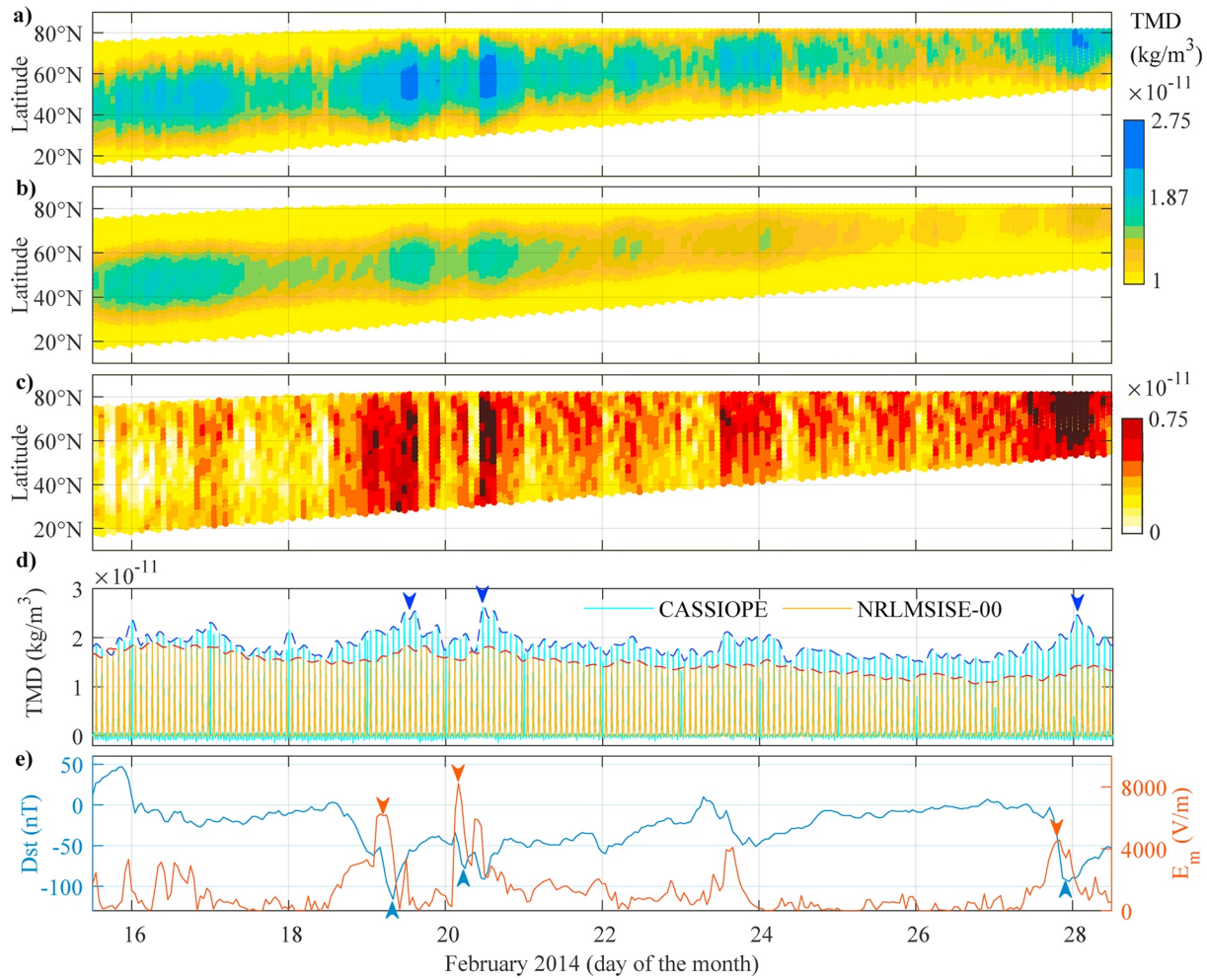

Figure 5. TMD estimates below 400 km altitude from (a) CASSIOPE's precise orbits and from (b) NRLMSISE-00 during the second half of February 2014. The differences are shown in (c). Similar to Figure 4, the upper bounds of TMD are plotted in (d). In (e), we show the merging electric field E_m and the disturbance storm time Dst index. CASSIOPE, CAScade SmallSat and IOnospheric Polar Explorer; TMD, thermospheric mass density.

estimates below 400 km altitude for the second half of February 2014. The differences between these figures are displayed in Figure 5c. This figure shows the limited performance of NRLMSISE-00 to localize and represent, with high resolution, the short-term variations, and small features during the different phases of the storm. Similar to Figure 4b, Figure 5d shows the upper bounds of TMD (lowest altitude) as described by CASSIOPE and NRLMSISE-00. In this figure, both CASSIOPE and NRLMSISE-00 upper-bounds display similar values previous to the storm (15–18 February), but afterward a clear bias develops as the storm gets more complex. This feature suggests that NRLMSISE-00 underestimates the recovery phase of highly complex, multiphase geomagnetic storms.

Finally, Figure 6 shows the lag-time Pearson linear correlation coefficients for both CASSIOPE and NRLMSISE-00 upper bounds of TMD (lowest altitude) with respect to the E_m index. In this analysis, we employ the second half of February 2014, and apply a lag-time range of ±18 h. The maxima correlation corresponds to CASSIOPE with 72.4% at a time delay of 7.5 h. These results agree very well with the reported values of Calabia and Jin (2019) for the northern hemisphere. On the other hand, NRLMSISE-00 shows a maxima correlation of 42.1%, with a time delay of 9.3 h. Besides the poor correlation to the E_m index, these results also suggest that NRLMSISE-00 retards the actual TMD responses in about 1.8 h.

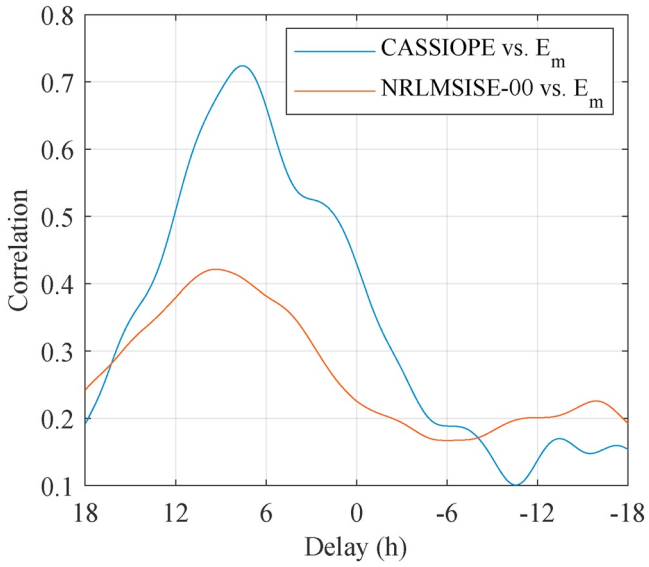

Figure 6. Delay/correlation for CASSIOPE and NRLMSISE-00 upper bounds of TMD (lowest altitude) with respect to the E_m index. CASSIOPE, CAScade SmallSat and IOnospheric Polar Explorer; TMD, thermospheric mass density.

4. Conclusions

We have examined the efficacy of TMD estimation using CASSIOPE's precise orbit position and velocity derived from GNSS measurements, and the results can confirm the high resolution of the new TMD estimates. In this approach, "observed" air drag accelerations are computed through numerical differentiation of the precise velocities, so that gravitational and radiation pressure accelerations can be subsequently removed. Afterward, the resulting air drag accelerations allow the computation of high-cadence TMD estimates.

Due to the lack of direct C_D or TMD measurements for validation, we have approximated a variable C_D for the CASSIOPE satellite, and compared the resulting TMD estimates with that modeled by the NRLMSISE-00 model. In this study, the new TMD estimates from CASSIOPE GNSS receivers have shown a great potential to describe in detail the short-term variations caused by the February 2014 geomagnetic storm. TMD estimates from both CASSIOPE and NRLMSISE-00 have displayed similar values previous to the storm, but these started to disagree as the geomagnetic-storm disturbances evolved. Moreover, NRLMSISE-00 has exhibited to underestimate the recovery phase of this highly complex, multiphase geomagnetic storm. Finally, the correlation to the E_m index has confirmed the poor performance of NRLMSISE-00 to represent the TMD disturbances during this storm, and a time-lag of about 1.8 h.

Estimating high-resolution TMD is a very relevant topic, since the performance of existing models used in POD is limited, especially during geomagnetic-storm times. In this manuscript, we have demonstrated that the GNSS-derived TMD estimates of the CASSIOPE satellite are valuable observations to be used and investigated in numerous studies. TMD is essential for space technologies and research, but the existing measurement techniques fail in quantity and quality to develop accurate empirical models. Using this technique, TMD can be sensed at high-resolution from GNSS receivers, and this will provide numerous TMD data sets from other missions to improve the existing state-of-the-art. Future works are addressed, but not restricted, to improve the force models, to mitigate the signal noises, and to investigate the accuracy of a larger TMD data set. Finally, we highlight the need to increase the research efforts to accurately estimate or directly measure the actual TMD and/or drag coefficient C_D of satellites.

Data Availability Statement

The CASSIOPE precise orbit data are publicly available from https://epop-data.phys.ucalgary.ca and ftp://swarm-diss.eo.esa.int. The reflectivity data are available from the Total Ozone Mapping Spectrometer (TOMS) project, http://disc.sci.gsfc.nasa.gov/acdisc/TOMS. The space weather data are available from the website of the Low Resolution OMNI (LRO) data set of NASA, http://omniweb.gsfc.nasa.gov/form/dx1.html. The merging electric field E_m is computed with the NASA's space weather data following the indications of R. Liu et al. (2010). The geomagnetic data are available from the International Service of Geomagnetic Indices (ISGI), http://isgi.unistra.fr/data_download.php. All data supporting the findings of this study will be available upon request.

Acknowledgments
This work was supported by the National Natural Science Foundation of China-German Science Foundation (NSFC-DFG) Project (Grant No. 41761134092), the Startup Foundation for Introducing Talent of NUIST (Grant No. 2243141801036), and the Talent Start-Up Funding project of NUIST (Grant No. 1411041901010). Great appreciation is extended to ESA's Swarm mission and to CASSIOPE/e-POP team at the University of Calgary for providing the precise orbit data, and to NASA and ISGI for the space weather and geomagnetic indices. The authors are very thankful to the anonymous reviewers, Dr. Liu Jiandong, Ms. Catherine M Jones, and Ms. Yijie Ning for their revisions and suggestions to improve a previous version of the manuscript.

References

Aikin, A. C., Hedin, A. E., Kendig, D. J., & Drake, S. (1993). Thermospheric molecular oxygen measurements using the ultraviolet spectrometer on the solar maximum mission spacecraft. *Journal of Geophysical Research*, *98*(A10), 17607–17613. https://doi.org/10.1029/93JA01468

Anderson, R. L., Born, G. H., & Forbes, J. M. (2009). Sensitivity of orbit predictions to density variability. *Journal of Spacecraft and Rockets*, *46*(6), 1214–1230. https://doi.org/10.2514/1.42138

Bhanderi, D. (2005). *Spacecraft attitude determination with Earth albedo corrected Sun sensor measurements* (Dissertation). Aalborg University. https://doi.org/10.2514/6.2005-6465

Bowman, B. R., Tobiska, W. K., Marcos, F. A., Huang, C. Y., Lin, C. S., & Burke, W. J. (2008). *A new empirical thermospheric density model JB2008 using new solar and geomagnetic indices*. AIAA/AAS Astrodynamics Specialist Conference and Exhibit, 18–21 August 2008, Honolulu, Hawaii AIAA 2008–6438. https://doi.org/10.2514/6.2008-6438

Bruinsma, S. L. (2015). The DTM-2013 thermosphere model. *Journal of Space Weather and Space Climate*, *5*, A1. https://doi.org/10.1051/swsc/2015001

Bruinsma, S. L., Doornbos, E., & Bowman, B. R. (2014). Validation of GOCE densities and evaluation of thermosphere models. *Advances in Space Research*, *54*, 576–585. https://doi.org/10.1016/j.asr.2014.04.008

Bruinsma, S. L., Tamagnan, D., & Biancale, R. (2004). Atmospheric densities derived from CHAMP/STAR accelerometer observations. *Planetary and Space Science*, *52*, 297–312. https://doi.org/10.1016/j.pss.2003.11.004

Calabia, A., & Jin, S. (2016). New modes and mechanisms of thermospheric mass density variations from GRACE accelerometers. *Journal of Geophysical Research: Space Physics*, *121*(11), 191–11. https://doi.org/10.1002/2016JA022594

Calabia, A., & Jin, S. (2017). Thermospheric density estimation and responses to the March 2013 geomagnetic storm from GRACE GPS-determined precise orbits. *Journal of Atmospheric and Solar-Terrestrial Physics*, *154*, 167–179. https://doi.org/10.1016/j.jastp.2016.12.011

Calabia, A., & Jin, S. (2019). Solar cycle, seasonal, and asymmetric dependencies of thermospheric mass density disturbances due to magnetospheric forcing. *Annales Geophysicae*, *37*, 989–1003. https://doi.org/10.5194/angeo-37-989-2019

Calabia, A., Jin, S., & Tenzer, R. (2015). A new GPS-based calibration of GRACE accelerometers using the arc-to-chord threshold uncovered sinusoidal disturbing signal. *Aerospace Science and Technology*, *45*, 265–271. https://doi.org/10.1016/j.ast.2015.05.013

Calabia, A., Tang, G., & Jin, S. (2020). Assessment of new thermospheric mass density model using NRLMSISE-00 model, GRACE, Swarm-C, and APOD observations. *Journal of Atmospheric and Solar-Terrestrial Physics*, *199*, 105207. https://doi.org/10.1016/j.jastp.2020.105207

Chen, G.-m., Xu, J., Wang, W., & Burns, A. G. (2014). A comparison of the effects of CIR- and CME-induced geomagnetic activity on thermospheric densities and spacecraft orbits: Statistical studies. *Journal of Geophysical Research: Space Physics*, *119*, 7928–7939. https://doi.org/10.1002/2014JA019831

Clemmons, J. H., Hecht, J. H., Salem, D. R., & Strickland, D. J. (2008). Thermospheric density in the Earth's magnetic cusp as observed by the Streak mission. *Geophysical Research Letters*, *35*, L24103. https://doi.org/10.1029/2008GL035972

Cnossen, I., & Förster, M. (2016). North-south asymmetries in the polar thermosphere-ionosphere system: Solar cycle and seasonal influences. *Journal of Geophysical Research: Space Physics*, *121*, 612–627. https://doi.org/10.1002/2015JA021750

Desai, S. D. (2002). Observing the pole tide with satellite altimetry. *Journal of Geophysical Research*, *107*(C11), 3186. https://doi.org/10.1029/2001JC001224

Determan, J. R., Budzien, S. A., Kowalski, M. P., Lovellette, M. N., Ray, P. S., Wolff, M. T., et al. (2007). Measuring atmospheric density with X-ray occultation sounding. *Journal of Geophysical Research*, *112*, A06323. https://doi.org/10.1029/2006JA012014

Doornbos, E. (2012). *Thermosphere density and wind determination from satellite dynamics* (Dissertation). Springer Nature. https://doi.org/10.1007/978-3-642-25129-0

Doornbos, E., van den IJssel, J., Luhr, H., Forster, M., & Koppenwallner, G. (2010). Neutral density and crosswind determination from arbitrarily oriented multiaxis accelerometers on satellites. *Journal of Spacecraft and Rockets*, *47*(4), 580–589. https://doi.org/10.2514/1.48114

Drob, D. P., Emmert, J. T., Meriwether, J. W., Makela, J. J., Doornbos, E., Conde, M., et al. (2015). An update to the Horizontal Wind Model (HWM): The quiet time thermosphere. *Earth and Space Science*, *2*, 301–319. https://doi.org/10.1002/2014EA000089

Emmert, J. T. (2015). Thermospheric mass density: A review. *Advances in Space Research*, *56*, 773–824. https://doi.org/10.1016/j.asr.2015.05.038

Emmert, J. T., & Picone, J. M. (2010). Climatology of globally averaged thermospheric mass density. *Journal of Geophysical Research*, *115*, A09326. https://doi.org/10.1029/2010JA015298

Ercha, A., Ridley, A. J., Zhang, D. & Xiao, D. Z. (2012). Analyzing the hemispheric asymmetry in the thermospheric density response to geomagnetic storms. *Journal of Geophysical Research*, *117*, A08317. https://doi.org/10.1029/2011JA017259

Frommknecht, B. (2008). *Integrated sensor analysis of the GRACE mission*. DGK, Reihe C, Heft 617, Verlag der Bayerischen Akademie der Wissenschaften.

Gonzalez, W. D., Tsurutani, B. T., & Clúa de Gonzalez, A. L. (1999). Interplanetary origin of geomagnetic storms. *Space Science Reviews*, *88*, 529–562. https://doi.org/10.1023/a:1005160129098

Guo, J., Wei, F., Feng, X., Liu, H., Wan, W., Yang, Z., et al. (2016). Alfvén waves as a solar-interplanetary driver of the thermospheric disturbances. *Scientific Reports*, *6*, 18895. https://doi.org/10.1038/srep18895

IJssel, J. v. d. (2014). *GPS-based precise orbit determination and accelerometry for low flying satellites* (Dissertation). TU Delft.

Ijssel, J. v. d., & Visser, P. (2007). Performance of GPS-based accelerometry: CHAMP and GRACE. *Advances in Space Research*, *39*, 1597–1603. https://doi.org/10.1016/j.asr.2006.12.027

Jin, S., Calabia, A., & Yuan, L. (2018). *Thermospheric variations from GNSS and accelerometer measurements on small satellites* (Vol. 106, pp. 484–495). Proceedings of IEEE. https://doi.org/10.1109/JPROC.2018.2796084

Jin, S., & Su, K. (2020). PPP models and performances from single- to quad-frequency BDS observations. *Satellite Navigation*, *1*(1), 16. https://doi.org/10.1186/s43020-020-00014-y

Kim, D., & Langley, R. B. (2019). The GPS attitude, positioning, and profiling experiment for the enhanced polar outflow probe platform on the Canadian CASSIOPE satellite. *Geomatica*, *64*(2), 233–243. https://doi.org/10.5623/geomat-2010-0023

Knocke, P., & Ries, J. (1987). *Earth radiation pressure effects on satellites*. Center for Space Research, Technical Memorandum, CSR-TM-87-01, The University of Texas at Austin.

Kuang, D., Desai, S., & Pi, A. X. (2014). Measuring atmospheric density using GPS-LEO tracking data. *Advances in Space Research*, *53*(2), 243–256. https://doi.org/10.1016/j.asr.2013.11.022

Lei, J., Thayer, J. P., & Forbes, J. M. (2010). Longitudinal and geomagnetic activity modulation of the equatorial thermosphere anomaly. *Journal of Geophysical Research*, *115*, A08311. https://doi.org/10.1029/2009JA015177

Lei, J., Thayer, J. P., Wang, W., Luan, X., Dou, X., & Roble, R. (2012). Simulations of the equatorial thermosphere anomaly: Physical mechanisms for crest formation. *Journal of Geophysical Research*, *117*, A06318. https://doi.org/10.1029/2012JA017613

Lianglian, Y., Jin, S. G., & Calabia, A. (2019). Distinct thermospheric mass density variations following the September 2017 geomagnetic storm from GRACE and Swarm. *Journal of Atmospheric and Solar-Terrestrial Physics*, *184*, 30–36.

Liu, H., Yamamoto, M., & Lühr, H. (2009). Wave-4 pattern of the equatorial mass density anomaly: A thermospheric signature of tropical deep convection. *Geophysical Research Letters*, *36*, L18104. https://doi.org/10.1029/2009GL039865

Liu, R., Lühr, H., Doornbos, E., & Ma, S.-Y. (2010). Thermospheric mass density variations during geomagnetic storms and a prediction model based on the merging electric field. *Annales Geophysicae*, *28*, 1633–1645. https://doi.org/10.5194/angeo-28-1633-2010
Liu, R., Ma, S.-Y., & Lühr, H. (2011). Predicting storm-time thermospheric mass density variations at CHAMP and GRACE altitudes. *Annales Geophysicae*, *29*, 443–453. https://doi.org/10.5194/angeo-29-443-2011
Luthcke, S. B., Marshall, J. A., Rowton, S. C., Rachlin, K. E., Cox, C. M., & Williamson, R. G. (1997). Enhanced radiative force modeling of the tracking and data relay satellites. *Journal of the Astronautical Sciences*, *45*(3), 349–370. https://doi.org/10.1007/bf03546409
March, G., Visser, T., Visser, P. N. A. M., & Doornbos, E. N. (2019). CHAMP and GOCE thermospheric wind characterization with improved gas-surface interactions modelling. *Advances in Space Research*, *64*(6), 1225–1242. https://doi.org/10.1016/j.asr.2019.06.023
Mayer-Gürr, T., Savcenko, R., Bosch, W., Daras, I., & Dahle, F. C. (2012). Ocean tides from satellite altimetry and GRACE. *Journal of Geodynamics*, *59–60*, 28–38. https://doi.org/10.1016/j.jog.2011.10.0010.1016/j.jog.2011.10.009
McLaughlin, C. A., Lechtenberg, T., Fattig, E., & Krishna, D. M. (2013). Estimating density using precision satellite orbits from multiple satellites. *Journal of the Astronautical Sciences*, *59*(1–2), 84–100. https://doi.org/10.1007/s40295-013-0007-4
Mehta, P. M., Walker, A., McLaughlin, C. A., & Koller, J. (2014). Comparing physical drag coefficients computed using different gas-surface interaction models. *Journal of Spacecraft and Rockets*, *51*, 873–883. https://doi.org/10.2514/1.a32566
Meier, R. R., & Picone, J. M. (1994). Retrieval of absolute thermospheric concentrations from the far UV dayglow: An application of discrete inverse theory. *Journal of Geophysical Research*, *99*, 6307–6320. https://doi.org/10.1029/93JA02775
Meier, R. R., Picone, J. M., Drob, D., Bishop, J., Emmert, J. T., Lean, J. L., et al. (2015). Remote sensing of Earth's limb by TIMED/GUVI: Retrieval of thermospheric composition and temperature. *Earth and Space Science*, *2*, 1–37. https://doi.org/10.1002/2014EA000035
Montenbruck, O., & Gill, E. (2013). *Satellite orbits: Models, methods and applications*. Springer.
Montenbruck, O., Hauschild, A., Langley, R. B., & Siemes, C. (2019). CASSIOPE orbit and attitude determination using commercial off-the-shelf GPS receivers. *GPS Solutions*, *23*(114). https://doi.org/10.1007/s10291-019-0907-2
Müller, S., Lühr, H., & Rentz, S. (2009). Solar and magnetospheric forcing of the low latitude thermospheric mass density as observed by CHAMP. *Annales Geophysicae*, *27*, 2087–2099. https://doi.org/10.5194/angeo-27-2087-2009
Newton, I. (1726). *Philosophiæ naturalis principia mathematica*. Harvard UP.
Nicolls, M. J., Bahcivan, H., Häggström, I., & Rietveld, M. (2014). Direct measurement of lower thermospheric neutral density using multifrequency incoherent scattering. *Geophysical Research Letters*, *41*, 8147–8154. https://doi.org/10.1002/2014GL062204
Panzetta, F., Bloßfeld, M., Erdogan, E., Rudenko, S., Schmidt, M., & Müller, H. (2018). Towards thermospheric density estimation from SLR observations of LEO satellites: A case study with ANDE-Pollux satellite. *Journal of Geodesy*, *93*(3), 353–368. https://doi.org/10.1007/s00190-018-1165-8
Pardini, C., Tobiska, W. K., & Anselmo, L. (2006). Analysis of the orbital decay of spherical satellites using different solar flux proxies and atmospheric density models. *Advances in Space Research*, *37*(2), 392–400. https://doi.org/10.1016/j.asr.2004.10.009
Petit, G., & Luzum, B. (2010). *IERS conventions (2010), IERS technical note 36, International Earth Rotation and Reference Systems Service (IERS)*. Verlag des Bundesamts für Kartographie und Geodäsie.
Picone, J. M., Emmert, J. T., & Lean, J. L. (2005). Thermospheric densities derived from spacecraft orbits: Accurate processing of two-line element sets. *Journal of Geophysical Research*, *110*, A03301. https://doi.org/10.1029/2004ja010585
Picone, J. M., Hedin, A. E., Drob, D. P., & Aikin, A. C. (2002). NRLMSISE-00 empirical model of the atmosphere: Statistical comparisons and scientific issues. *Journal of Geophysical Research*, *107*(A12), 15–1. https://doi.org/10.1029/2002JA009430
Santoni, F., Piergentili, F., & Graziani, F. (2010). Broglio Drag Balance for neutral thermosphere density measurement on UNICubeSAT. *Advances in Space Research*, *45*(5), 651–660. https://doi.org/10.1016/j.asr.2009.10.001
Siemes, C., de Teixeira da Encarnação, J., Doornbos, E., van den IJssel, J., Kraus, J., Pereštý, R., et al. (2016). Swarm accelerometer data processing from raw accelerations to thermospheric neutral densities. *Earth, Planets and Space*, *68*(1), 92. https://doi.org/10.1186/s40623-016-0474-5
Sutton, E. K. (2008). *Effects of solar disturbances on the thermosphere densities and winds from CHAMP and GRACE satellite accelerometer data* (Dissertation). University of Colorado.
Sutton, E. K., Forbes, J. M., & Knipp, D. J. (2009). Rapid response of the thermosphere to variations in Joule heating. *Journal of Geophysical Research*, *114*, A04319. https://doi.org/10.1029/2008JA013667
Sutton, E. K., Nerem, R. S., & Forbes, J. M. (2007). Density and winds in the thermosphere deduced from accelerometer data. *Journal of Spacecraft and Rockets*, *44*(6), 1210–1219. https://doi.org/10.2514/1.28641
Tang, G., Li, X., Cao, J. S. L., Liu, S., Chen, G., Man, H., et al. (2020). APOD mission status and preliminary results. *Science China Earth Sciences*, *63*, 257–266. https://doi.org/10.1007/s11430-018-9362-6
Tapley, B. D., Schutz, B. E., & Born, G. H. (2004). *Statistical orbit determination*. Elsevier, Academic press.
Vielberg, K., & Kusche, J. (2020). Extended forward and inverse modeling of radiation pressure accelerations for LEO satellites. *Journal of Geodesy*, *94*, 43. https://doi.org/10.1007/s00190-020-01368-6
Visser, P., Doornbos, E., van den IJssel, J., & Teixeira da Encarnação, J. (2013). Thermospheric density and wind retrieval from Swarm observations. *Earth, Planets and Space*, *65*, 1319–1331. https://doi.org/10.5047/eps.2013.08.003
Walker, A., Mehta, P., & Koller, J. (2014). Drag coefficient model using the Cercignani-Lampis-Lord gas-surface interaction model. *Journal of Spacecraft and Rockets*, *51*(5), 1544–1563. https://doi.org/10.2514/1.A32677
Wöske, F., Kato, T., Rievers, B., & List, M. (2019). GRACE accelerometer calibration by high precision non-gravitational force modeling. *Advances in Space Research*, *63*(3), 1318–1335. https://doi.org/10.1016/j.asr.2018.10.025